Carbon Trends 5 (2021) 100088

Contents lists available at ScienceDirect

Carbon Trends

journal homepage: www.elsevier.com/locate/cartre

Physical and chemical mechanisms that influence the electrical conductivity of lignin-derived biochar

Seth Kane[a], Rachel Ulrich[b], Abigail Harrington[c], Nicholas P. Stadie[c], Cecily Ryan[a,*]

[a] Mechanical and Industrial Engineering Dept. & Center for Biofilm Engineering Montana State University, Bozeman, MT 59717, United States
[b] Department of Mathematical Sciences Montana State University, Bozeman, MT 59717, United States
[c] Department of Chemistry and Biochemistry Montana State University, Bozeman, MT 59717, United States

ARTICLE INFO

Article history:
Received 28 July 2021
Accepted 30 July 2021

Keywords:
Biochar conductivity
Lignin
Carbon powders
Sustainable electronics
Carbon-based electronics

ABSTRACT

Lignin-derived biochar is a promising, sustainable alternative to petroleum-based carbon powders (e.g., carbon black) for polymer composite and energy storage applications. Prior studies of these biochars demonstrate that high electrical conductivity and good capacitive behavior are achievable. However, these studies also show high variability in electrical conductivity between biochars ($\sim 10^{-2}$–10^{2} S/cm). The underlying mechanisms that lead to desirable electrical properties in these lignin-derived biochars are poorly understood. In this work, we examine the causes of the variation in conductivity of lignin-derived biochar to optimize the electrical conductivity of lignin-derived biochars. To this end, we produced biochar from three different lignins, a whole biomass source (wheat stem), and cellulose at two pyrolysis temperatures (900 °C, 1100 °C). These biochars have a similar range of conductivities (0.002 to 18.51 S/cm) to what has been reported in the literature. Results from examining the relationship between chemical and physical biochar properties and electrical conductivity indicate that decreases in oxygen content and changes in particle size are associated with increases in electrical conductivity. Importantly, high variation in electrical conductivity is seen between biochars produced from lignins isolated with similar processes, demonstrating the importance of the lignin's properties on biochar electrical conductivity. These findings indicate how lignin composition and processing may be further selected and optimized to target specific applications of lignin-derived biochars.

1. Introduction

Carbon black is an amorphous graphitic carbon powder that has developed as an essential filler for thermally and electrically conductive composites [1,2]. Carbon black's excellent electrical conductivity, low percolation threshold, and low cost make carbon black an ubiquitous additive to create electrically conductive composite materials for polymer composite and energy storage applications [1,3–6]. The development of replacements for carbon black from renewable feedstocks, such as biomass, could improve the sustainability of these important applications. It is critical to understand and control the synthesis parameters that increase electrical conductivity of carbon materials derived from these alternate sources in order to develop renewable alternatives to carbon black.

One promising renewable feedstock for the production of carbon filler materials is lignin. Lignin is a primary component of woody biomass, an abundant biopolymer, and a waste product of papermaking and bio-ethanol industries, with over 50 million metric tons isolated each year [7]. Due to lignin's aromatic carbon monomer backbone, waste sourcing, and low cost it has potential as an ideal precursor for renewable alternatives to carbon black [8]. Lignin can be pyrolyzed to form biochar, a carbon-rich material most typically applied as a soil amendment [9]. Depending on processing conditions and source, lignin-derived biochar can be produced with properties similar to those of carbon black [10,11] including small particle sizes [12], high electrical conductivity [13], and strong capacitance [14].

A review of past studies shows high variability in biochar electrical conductivity. Biochars produced at 900 °C have been found to have electrical conductivities ranging from 1.91×10^{-5} S/cm to 62.96 S/cm (Fig. 1) [10,13–35]. For reference, a typical range of conductivities observed for carbon black is shown as the grey region between 0.5 and 12 S/cm in Fig. 1. Differing pyrolysis temperatures, feedstocks, preprocessing conditions, heating rates, and catalysts used may impact the electrical conductivity of biochar. When

* Corresponding author.
E-mail address: cecily.ryan@montana.edu (C. Ryan).

https://doi.org/10.1016/j.cartre.2021.100088

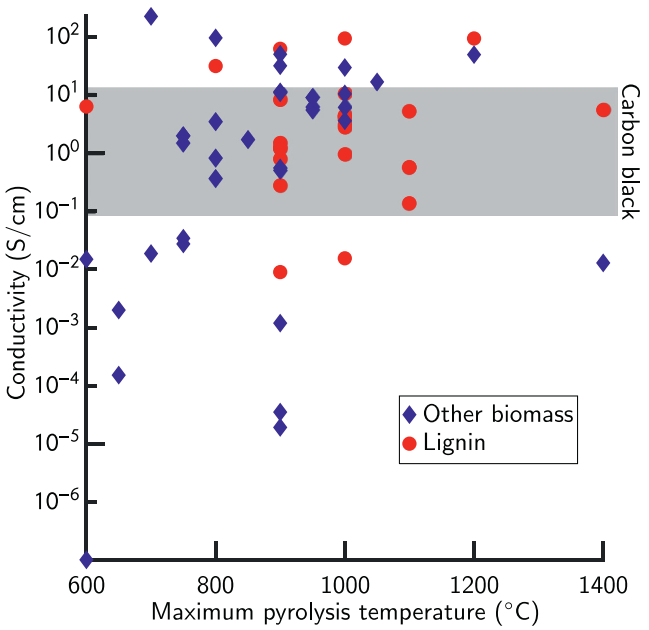

Fig. 1. A review of literature values for biochar produced from lignin (red ●) and other biomass (blue ♦) [10,13–35]. The grey box shows a range of typical carbon black conductivities, independent of processing temperature [34,36]. Additional information on these biochar conductivity data is shown in Table S1. (For interpretation of the references to colour in this figure legend, the reader is referred to the web version of this article.)

examining only lignin-derived biochars, a wide range of conductivities is still observed, with conductivities of biochar produced at 900 °C ranging from 0.009 S/cm to 62.96 S/cm. Past studies have proposed differences in metal content [10,20], oxygen content [10], surface area [10], density [27], carbon content [28] and the size of the graphitic crystallites [19,23] as factors influencing conductivity. However, to our knowledge, no study to date has systematically examined the mechanisms behind the observed differences in electrical conductivity in biochar. Understanding the mechanisms that govern conductivity in biomass-derived carbon electronics, including lignin, is necessary to optimize biochar as an alternative to carbon black in electrically conductive applications.

In this study, we examine the relationship between lignin sourcing and the electrical conductivity of lignin-derived biochar. We hypothesized that lignin sourcing would have a significant impact on biochar properties, and in particular electrical conductivity. Biochar was produced from three lignins: alkaline lignin, dealkaline lignin, and a laboratory isolated lignin. To keep biochar processing consistent, biochar was produced at maximum pyrolysis temperatures of 900 °C and 1100 °C. To build a better understanding of the relationship between biochar properties and electrical conductivity, we characterized the physical and chemical properties of the biochar and measured the electrical conductivity of each biochar. We then explored the relationship between lignin sourcing, biochar properties, and the resulting biochar's electrical conductivity. This research identifies key directions of future work to improve the electrical conductivity of biochar and supports the development of conductive biochar as a renewable alternative to carbon black.

2. Methods and materials

2.1. Materials

Three different lignins were used as biochar feedstocks to examine variations between different lignin processing conditions.

Table 1
Biochar production variables and abbreviations.

	Pyrolysis Temperature	
Feedstock	900 °C	1100 °C
Alkaline Lignin	AL900	AL1100
Dealkaline Lignin	DAL900	DAL1100
Hodge Lab Lignin	HL900	HL1100
Wheat Stem	WS900	WS1100
Cellulose	CELL900	CELL1100[†]

[†] No biochar was produced from cellulose at 1100 °C due to low pyrolysis yields.

Alkaline and dealkaline lignins were purchased from TCI America (product # L0082 and L0045 respectively, Portland, OR, USA). Both TCI lignins are isolated from wood via a sodium sulfite (Na_2SO_3) treatment, followed by chemical modifications, including desulfonation, oxidation, hydrolysis, and demethylation. These lignins differ in that alkaline lignin has been treated after isolation to have a pH between 8 and 10 [37]. Laboratory isolated lignin was provided by the Hodge Research Group (Montana State University, Bozeman, MT, USA). This lignin is isolated from poplar wood by an alkaline pre-extraction process followed by acidification with sulfuric acid [38].

In addition to lignins, biochar was produced from non-lignin biomass sources. Solid stem wheat stem feedstock was provided by the Montana State University Agricultural Research and Teaching Farm (Bozeman, MT, USA). Cellulose feedstock was purchased from Sigma-Aldrich (Fibrous, medium, product #C6288, St. Louis, MO, USA). All biochar feedstocks were stored in a drying oven at 105 °C until use.

2.2. Biochar production

Lignin, biomass, and cellulose feedstocks for biochar production were ball milled to reduce particle size. Ball milling was performed with zirconia media at 60 rpm (1 Hz), for 24 h for lignins and cellulose, and 72 h for wheat stems. After milling, feedstocks were stored in a drying oven at 105 °C for at least 24 h before pyrolysis.

Biochar was produced by slow pyrolysis in a Thermo Fisher Lindberg/Blue M Mini-Mite tube furnace with an alumina tube and alumina boat as described by Quosai et al. (2018) [17] and Arroyo et al. (2018, 2019) [39,40]. Nitrogen was flowed through the tube at 100 mL/min for 10 min before heating and at 30 mL/min during heating. The furnace temperature ramp was 10 °C/min to a maximum temperature of 900 °C or 1100 °C. The maximum temperature was maintained for 1 h and then cooled to room temperature. All biochars were ball milled in a Retsch Mixer Mill 400 for 2.5 min at 30 Hz after pyrolysis to reduce clumping and then stored in a drying oven at 105 °C until use. A complete list of biochar production variables and abbreviations is shown in Table 1. Due to low biochar yields at 1100 °C, cellulose was only used to produce biochar at 900 °C.

2.3. Volume conductivity and impedance spectra

Volume conductivity is the primary material property of interest for electrically conductive filler materials. The volume conductivity of biochars was determined on a guard electrode compression fixture described by Kane et al. [34]. Volume conductivity measurements were performed on a Keithley 2450 Sourcemeter, with an applied current of 100 mA. For each biochar, 200 mg of biochar was placed in the sample holder, and resistance measurements were taken every 0.127 cm (0.05 in) of thickness from the point of the first contact until no more pressure could be applied. A settling period of 30 s was used, and measurements between 25

and 31 s were selected for use. Five measurements were taken of the same sample of each biochar, with an average of 100 resistance readings taken for each measurement.

To better characterize the electrical behavior of the biochar, electrical impedance spectra were collected with the same guard electrode compression fixture and a Hioki 3533-01 LCR meter. Impedance spectra were collected on 200 mg of biochar every 0.127 cm (0.05 in) from the point where 0.1 μA could be passed through the sample until no more pressure could be applied.

2.4. Characterization of biochar chemical structure

2.4.1. Thermogravimetric infrared spectroscopy

Thermogravimetric analysis combined with infrared spectroscopy (TGA-IR) was performed on the biochar feedstocks to examine the pyrolysis reactions and the differences in pyrolysis rates between the different lignin feedstocks. TGA-IR was performed on a TA Instruments Q5000 IR and a Thermofisher Nicolet iS10 FTIR Spectrometer with a TGA-IR module. Samples were 20 mg and were ramped at 10 °C/min to 1100 °C under a nitrogen flow of 30 mL/min, mimicking pyrolysis conditions. The transport tube and IR gas cell were maintained at 300 °C to prevent condensation of gases. IR spectra were collected with a resolution of 8 cm^{-1} and six scans per measurement, between 500 and 4000 cm^{-1}.

2.4.2. Elemental composition

Energy-dispersive X-ray spectroscopy (EDX) was performed to determine the elements present in the biochar. A JEOL JSM-6100 scanning electron microscope with a RÖNTEC XFlash 1000 energy-dispersive X-ray detector was used to collect the spectra and for imaging, with an electron beam energy of 20 kV. Biochar samples were placed on carbon sticky dots (product #16084-3, Ted Pella Inc., Redding, CA, USA) and sputter coated with iridium on an Emitech K-875X sputter coater at 30 mA for 60 s.

Combustion analysis was performed to measure the C, H, N, and S elemental composition of the biochar. Combustion analysis was performed and analyzed in duplicate by Atlantic Microlab Inc. (Norcross, Georgia, USA).

Based on the results of the EDX measurements, Na, Mg, Ca, and K were selected for inductively coupled plasma optical emission spectroscopy (ICP-OES) measurements. Before measurement, samples were digested using 10 mL trace-metal grade concentrated nitric acid (Fisher Scientific, product #A509P500, Pittsburgh, PA USA) on a Mars6 iWave digester. Two heating cycles were run to 220 °C with a ramp time of 15 min, a hold time of 15 min, and under 800 psi of pressure. Diluted samples (see Table S2 for dilutions) and cation standards were run in a matrix of 2% HNO_3 on a SpectroBlue ICP-OES in axial view mode (high sensitivity).

Oxygen content was calculated as the remaining mass not quantified by combustion or ICP-OES analysis for AL, DAL, HL, and CELL feedstocks. For WS feedstocks, a silicon peak was observed via EDX analysis. Silicon (Si) content was quantified by multiplying the ratio of the peak intensity of the Si peak to the peak intensity of the C peak by the carbon content measured by combustion analysis. This silicon content was then subtracted from the remainder after combustion and ICP-OES analysis to determine the oxygen content in WS-derived biochars.

2.4.3. Attuned total reflectance Fourier transform infrared spectroscopy

Attuned total reflectance (ATR) Fourier transform infrared spectroscopy (FTIR) was performed to examine the functional groups of the biochar and their dependence on feedstock and pyrolysis temperature. ATR FTIR was performed using a Thermo Fisher Nicolet iS10 FTIR spectrometer with a Smart iTX ATR accessory with a diamond crystal. Spectra were collected between 600 and 4000 cm^{-1} at a resolution of 4 cm^{-1}, and with 64 scans for each biochar sample. Spectra were baseline corrected using OMNIC software (Thermo Fisher, v. 9.9.509) to account for baseline drift.

2.4.4. Raman spectroscopy

Raman spectroscopy was performed to investigate the graphitic content of each biochar sample using a Horiba LabRam HR Evolution NIR Raman microscope. Raman spectra were acquired with a 50× LWD objective, a stigmatic spectrometer with a grating of 1800 gr/mm, and a 532 nm 100 mW laser at 1–10% power. Raman spectra were collected between 1000 and 1800 cm^{-1}, corresponding to the region containing the G (~ 1580 cm^{-1}) and D (~ 1340 cm^{-1}) peaks [41,42].

Deconvolution of the Raman spectra was performed to determine D and G peak intensities. Deconvolution was performed in MATLAB (Mathworks inc., R2020a, v. 9.8.0.1380330) with the Curve Fitting Toolbox (v. 3.5.11). Spectra were fit with a Lorentzian lineshape for the D peak and a Breit-Wigner-Fano (BWF) lineshape for the G peak [42,43]. The D to G ratio I_{DG} was calculated as the intensity ratio of the D peak to the G peak in the best fit.

2.5. Characterization of biochar physical structure

2.5.1. Field emission scanning electron microscopy

Field emission scanning electron microscopy (FESEM) was performed to examine biochar particle size and surface and pore structure. Biochar was placed on carbon sticky dots (Ted Pella, product #16084-3), sputter coated with iridium, and examined on a Supra 55VP microscope at 1 kV and a working distance of approximately 6 mm with an SE2 detector.

2.5.2. Particle size analysis

Biochar particle size was measured using a Malvern Mastersizer 3000 particle size analyzer. Samples were dispersed in DI water, and the results were analyzed with the assumption of non-spherical particles.

2.5.3. Gas sorption for BET analysis

Nitrogen adsorption was measured at 77 K on all biochar samples using a Micromeritics 3-Flex sorption analyzer to determine the surface area and pore size distribution. Before testing, samples were degassed for 12 h at 150 °C under oil-free vacuum to 10^{-8} mbar. Approximately 0.3-2 g of each sample was subjected to nitrogen adsorption and desorption between $P/P_0 = 10^{-7}$ to 0.95 at 77 K. The results were fit to the Brunauer-Emmett-Teller (BET) model [44] to determine specific surface area using standard consistency criteria for microporous solids [45]. A non-local density functional theory (NLDFT) carbon slit pore model was used to determine the pore size distribution using Micromeritics Microactive software. Gas adsorption isotherms are shown in Figure S9.

2.6. Statistical methods

Statistical analyses were conducted in the R software environment (R Core Team, version 4.0.3, 2020) [46]. Contrasts were estimated using the emmeans package [47], a linear mixed-effects model was estimated, and results visualized using the lmerTest package [48] and effects package [49], respectively. Five pseudo-replicate measurements of electrical conductivity were taken on a single sample of each biochar as described in Section 2.3. Since cellulose feedstock processed at 1100 °C did not yield any measurable biochar, an analysis of variance (ANOVA) was conducted on nine treatment levels of temperature and feedstock combinations (see supplemental information Section S1.2 for additional details on the ANOVA process). As a follow-up analysis, Bonferroni-corrected comparisons of interest were explored.

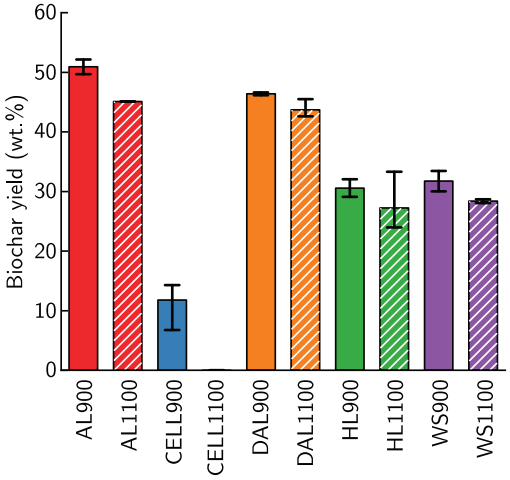

Fig. 2. Biochar production yield by biochar type. Bars represent the mean yield of all recorded runs, and error bars indicate maximum and minimum values. No solid mass remained after pyrolysis of cellulose at 1100 °C; therefore, it was not included in the remainder of the study.

The relationship between biochar chemical and physical properties and electrical conductivity was explored using a forward, step-wise *p*-value model selection process. The following variables were each considered for inclusion in the final model: surface area, oxygen-to-carbon (O:C) molar ratio, hydrogen-to-carbon (H:C) molar ratio, inorganic content (sum of Na, S, Mg, Ca, and K content), and average I_{DG}. Due to issues with multicollinearity, the variables carbon content and O:C molar ratio could not both be included in the model, and carbon content was removed. The response variable, maximum electrical conductivity (σ_{max}), necessitated a square-root transformation. Nested random effects were used for treatment ($i =$ AL900, AL1100, DAL900, DAL1100, CELL900, HL900, WS900, WS1100), pseudo-replicates within treatment ($j = 1, 2 \ldots 5$), and time observation within pseudo-replicate ($k = 1, 2 \ldots 7$ for measurements at 25–31 s). Therefore this transformation is given as an equation for $\sqrt{\hat{\sigma}_{max,ijk}}$. A full description of this model is given in Supplemental Information Section S1.2, and the code used to generate the model is available [50].

3. Results and discussion

3.1. Biochar processing behavior

Biochar pyrolysis yields differed depending on the feedstock used and the maximum treatment temperature (Fig. 2). AL900 had the highest average yield at 50.9 wt.%, while CELL900 produced the lowest measurable yield, with an average yield of 10.0 wt.%. For all feedstocks, pyrolysis at 1100 °C yielded less biochar than pyrolysis of the same feedstock at 900 °C. Cellulose feedstocks were not examined at 1100 °C, as no measurable solid material remained after pyrolysis of cellulose at 1100 °C.

TGA-IR analyses simulating the pyrolysis process showed an initial decrease in weight between 70 °C and 110 °C in all feedstocks due to water loss (Fig. 3). Above this temperature range, the cellulose feedstock degrades in a single step beginning at approximately 300 °C, with a maximum slope at approximately 324 °C (Fig. 3, blue). By 600 °C, no solid char remained in CELL samples. This decomposition has previously been attributed to the degradation of the cellulose polymer into its constituent glucose monomers, followed by degradation of these monomers to CO, CO_2, H_2, CH_4, and other short volatile hydrocarbons [51]. IR spectroscopy of the gases produced during TGA shows a single, strong peak in the Gram-Schmidt spectra at approximately 30 min (300 °C). The IR

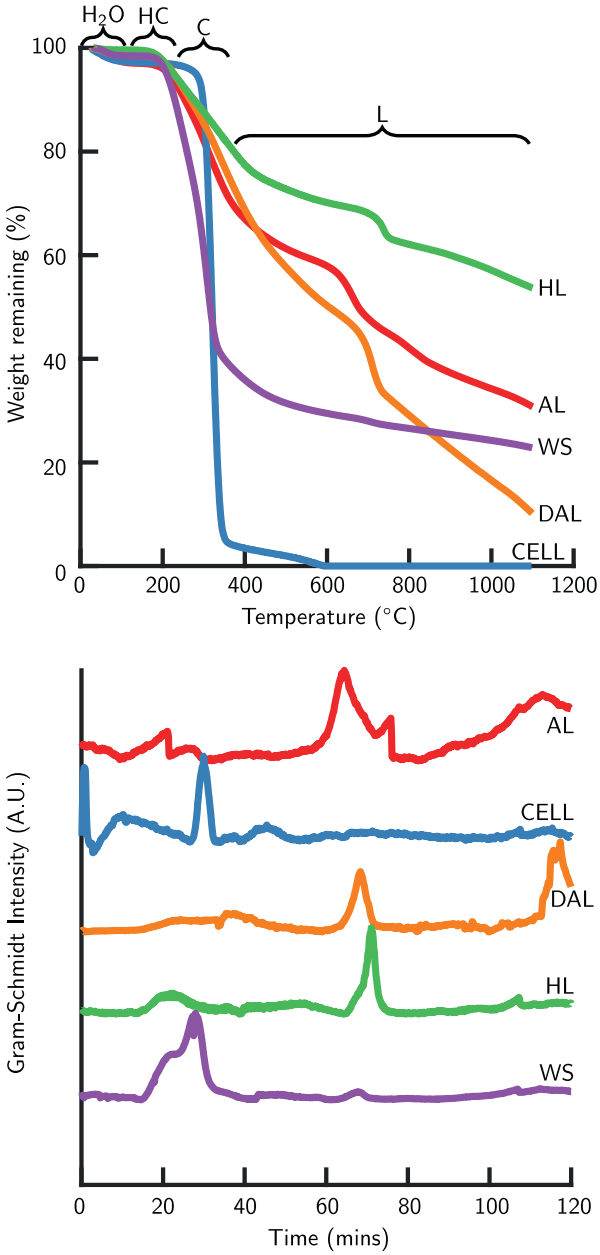

Fig. 3. (Top) TGA of all feedstocks to 1100 °C mimicking the production conditions of the biochar. Labeled temperature ranges correspond to the region used to identify: H_2O: evaporation of water, HC: degradation of hemicellulose, C: degradation of cellulose, and L: degradation of lignin. (Bottom) Stacked Graham-Schmidt spectra displaying the intensity of the full IR spectra during the above TGA curves. Accounting for the time delay for the gas to move between the TGA and IR, the TGA weight change and the evolution of peaks in the Grahm-Schmidt plot would be expected to align at a rate of 10 °C/min. Full three-dimensional representations of TGA-IR Data are available in the supplemental information.

spectra at 30 min support past findings, with peaks observed at 2368 cm^{-1} (CO_2), 1768 cm^{-1} (C=O), 2970 cm^{-1} (C-H) and 1242 cm^{-1} (C–O–C) (Figure S1) [51].

In contrast to cellulose, all lignin feedstocks show a slower degradation rate consistent with the expected behavior of the complex, aromatic carbon structure of lignin [51]. Two notable increases in slope can be seen in all lignins beginning between 180 and 220 °C and between 630 and 720 °C (Fig. 3, top). IR measurements of the gases released during TGA show CO_2 (2368 cm^{-1}) and CO (2185 cm^{-1}) to be released continuously from approximately 200 °C to 1100 °C for pyrolysis of all lignins, while C-O-

C and C=O peaks are observed at later time points, corresponding to the increase in TGA curve slope observed at approximately 700 °C (Figure S1). Neither TGA data nor IR measurements of gases released during TGA show meaningful differences between lignins beyond differences in weight loss.

Pyrolysis of WS involves a combination of these two mechanisms, consistent with the expected degradation of biomass comprised of cellulose, hemicellulose, and lignin. FTIR spectra at 30 min of WS pyrolysis products show the release of CO_2 (2368 cm^{-1}) and CO (2185 cm^{-1}), as well as additional hydrocarbons indicated by peaks corresponding to C-H (2933 cm^{-1}), C–O–C (1242 cm^{-1}) and C=O (1768 cm^{-1}) bonds [51] (Figure S1). Similar to CELL, TGA-IR spectra of WS show the release of C–O–C and C=O to happen together with CO_2 and CO after approximately 30 min. However, a second peak of C–O–C and C=O is seen at approximately 110 min, which may indicate that the lignin present in WS shows similar pyrolysis behavior to the isolated lignin.

TGA measurements show higher mass remaining than at the end of a biochar production run at the same temperature for most feedstocks. As TGA measurements did not include the 1 h dwell time included in biochar production, it is hypothesized that this increased time at the highest treatment temperature is the source of most observed differences. Additionally, during the production of HL biochars, it was observed that some solid char remained in the ceramic tube after the ceramic boat was removed and that much of the solid char remaining was above the rim of the ceramic boat containing the lignin. We hypothesize that this mass loss during the production of HL biochars in the tube furnace is the cause of the observed difference between production and TGA mass loss measurements. In contrast with other biochars, TGA measurements of CELL biochar show no solid mass remaining at 900 °C, while an average of 11.78% solid mass remained during biochar production. As the pyrolysis of cellulose is more endothermic than the pyrolysis of lignins [51], this increase in residual weight may be due to uneven heat transfer into the higher mass of cellulose used during biochar production than that used during TGA.

3.2. Biochar electrical conductivity

As a replacement for carbon black in carbon-based composites for energy storage applications, the primary material property of concern is electrical conductivity. All biochars show the expected conductivity s-curve, as the powder is compressed through its percolation threshold and transitions from insulating to conducting electrical behavior (Fig. 4), indicating that the full range of conductivity behavior was captured for these materials [34,52]. Small decreases in biochar conductivity are observed in some biochars following their peak, which has previously been attributed to the deformation of biochar particles with increased pressure after close packing has been achieved [34]. The maximum electrical conductivity of biochar in this study ranged from 0.002 S/cm for AL900 to 18.5 S/cm for HL1100. This range is similar to what has been observed in past literature for lignin-derived biochar produced between 900 °C and 1100 °C, which shows conductivity varying from 0.009 S/cm (Lignotech lignin, 900 °C [10]) and 95 S/cm (16% micro fibrillated cellulose and 84% lignosulfonate, 1000 °C [19]). The range of electrical conductivity measured indicates that the variation in electrical conductivity observed in past work is not solely due to variations in pyrolysis rate, added catalysts, and electrical conductivity measurement technique between studies, as these variables have been held constant in this study. The conductivity of HL1100 measured in this study is higher than has been previously reported for this same biochar [34]. This increase is attributed to reduced contact resistance from improvements in the polishing of the electrodes [53].

Table 2
Specific comparisons of interest for electrical conductivity of biochars. Two sets of comparisons are shown between different types of lignin pyrolyzed at 1100 °C (Lignin) and between each feedstock pyrolyzed at 1100 °C and 900 °C (Temp.).

	Comparison	Estimated difference[†] (S/cm)	*t*-statistic	*p*-value
Lignin	AL1100 - DAL1100	-2.81 ± 6.67	−1.2	1
	AL1100 - HL1100	-9.35 ± 6.67	−4	0.0021
	DAL1100 - HL1100	-6.54 ± 6.67	−2.8	0.0577
Temp.	AL1100 - AL900	1.26 ± 6.67	0.54	1
	DAL1100 - DAL900	2.02 ± 6.67	0.86	1
	HL1100 - HL900	8.12 ± 6.67	3.47	0.0095
	WS1100 - WS900	6.94 ± 6.67	2.97	0.0373

[†] Estimated differences represent the difference between the first and second listed biochar, and are reported with Bonferonni-corrected 95% confidence intervals.

An ANOVA, accounting for the random effects of sample and time observation, shows strong evidence for a difference in electrical conductivity for different biochars ($p < 0.001$). Pairwise comparisons indicate no evidence for a difference in electrical conductivity between AL1100 and DAL1100, suggesting that little difference in electrical conductivity exists between biochars produced from the two TCI lignins (AL and DAL) at 1100 °C (Table 2). When compared to biochar produced from laboratory isolated lignin (HL), biochar produced from both TCI lignins (AL and DAL) at 1100 °C show evidence for lower electrical conductivity (Table 2). This difference in electrical conductivity between lignins suggests that the post-isolation treatment of AL by TCI does not notably impact conductivity but that higher electrical conductivity can be obtained with other lignin isolation methods. Comparisons within each feedstock between pyrolysis temperatures of 900 °C and 1100 °C show almost no evidence for an increase in electrical conductivity for AL- or DAL-derived biochar with an increase in pyrolysis temperature. In contrast, WS-derived biochars show moderate evidence, and HL-derived biochars show strong evidence for an increase in electrical conductivity with an increase in pyrolysis temperature (Table 2). HL shows a larger estimated increase in conductivity from 900 °C to 1100 °C (+8.12 S/cm) than AL (+1.26 S/cm), DAL (+2.02 S/cm) or WS (+6.94 S/cm) feedstocks (Table 2). Possible mechanisms behind these differences between feedstocks are examined in more detail in Section 3.5.

All biochars measured in this study primarily show resistive AC electrical behavior (Fig. 5). At the point of highest compression, biochar impedance showed little frequency dependence. AL900, the highest impedance biochar, showed some capacitive behavior at high frequencies. In all biochars, some inductive behavior is observed at high frequencies. This inductive behavior has previously been attributed to poor shielding of connections and cables used in this experimental setup [34]. The AC electrical behavior observed for all biochars is consistent with results seen for biochar and carbon black in past work [34,54].

3.3. Biochar chemical characterization

The chemical composition of all biochars was measured to explore biochar constituents' role in biochar electrical conductivity. Combustion analysis showed a high percentage of carbon for all biochars, ranging from 60.7% for WS1100 to 92.2% for CELL900. In all lignin-derived biochars, carbon content increases as pyrolysis temperature increases from 900 °C to 1100 °C. HL-derived biochar shows higher carbon content at both 900 °C and 1100 °C than AL- or DAL-derived biochar, reaching a carbon content of 83.5% for HL1100. Hydrogen content was low for all biochars relative to their biomass feedstocks [51], with H:C molar ratios for lignin-derived biochars ranging from 0.13 for AL900 to 0.064 for HL1100. Simi-

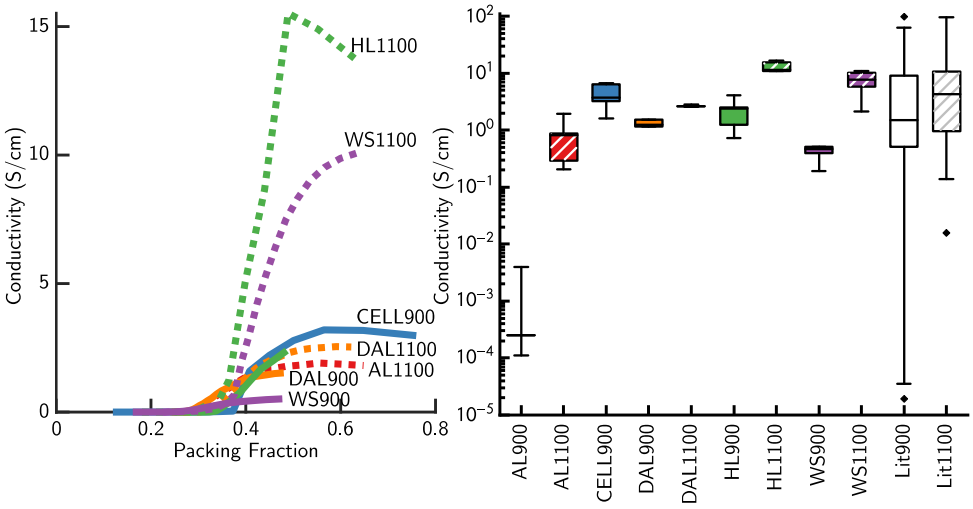

Fig. 4. (Left) Conductivity (σ) as a function of packing fraction for the first compression of all biochars examined. AL900 showed near-zero ($\sigma < 10^{-2}$) for all compressions and cannot be seen on the plot. (Right) Box plot of conductivity for all biochars examined in this study. Lit 900 and Lit 1100 represent biochars from the literature produced between 800–1000 and 1000–1200 °C, respectively. See Table S1 for a full summary of these biochars.

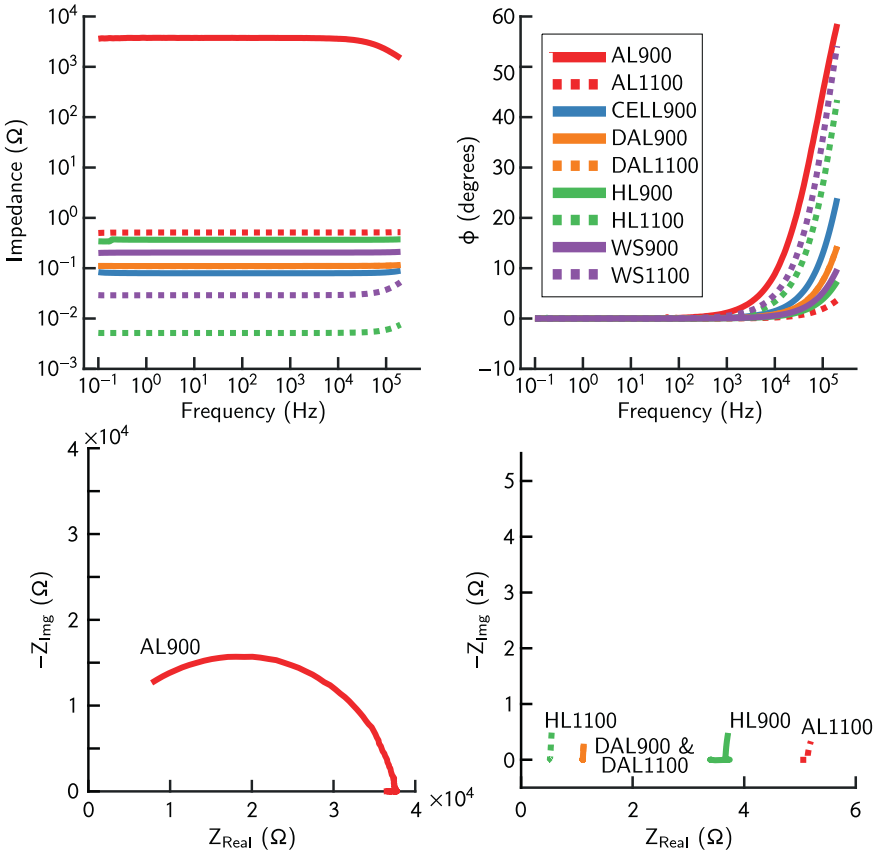

Fig. 5. (Top) Electrical impedance spectra for each biochar from 0.1 Hz to 200 kHz at the point of maximum compression. A Bode plot of impedance is shown on the left and phase shift (ϕ) on the right. (Bottom) Nyquist plots for electrical impedance spectra for (left) AL900 and (right) AL1100, DAL900, DAL1100, HL900 and HL1100 biochars. The limited imaginary component observed in all biochars except AL900 indicates a largely resistive response, while the semi-circular Nyquist plot of AL900 indicates capacitive behavior. Nyquist plots for WS900, WS1100, and CELL900 biochars are shown in Figure S2. (For interpretation of the references to colour in this figure legend, the reader is referred to the web version of this article.)

larly, O:C molar ratios decrease from 0.32 for AL900 to 0.08 for HL1100. All biochars measured in this study show higher hydrogen content at 900 °C than 1100 °C. The loss of hydrogen content with increasing pyrolysis temperature is expected to result in more graphitic biochars with higher pyrolysis temperatures.

High quantities of sulfur (S) and sodium (Na) are observed in all lignin-derived biochars. While AL- and DAL-derived biochars were observed to increase in S content with increasing pyrolysis temperature, HL-derived biochar decreased with 4.0% S at 900 °C and 2.5% S at 1100 °C. Na content decreased with rising pyrolysis temperatures for all lignin-derived biochars. Lower quantities

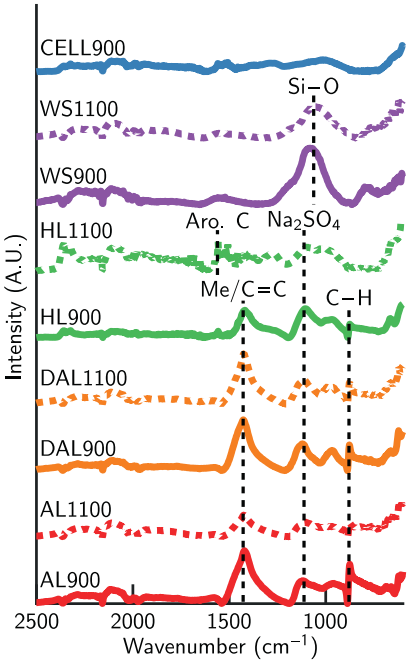

Fig. 6. Stacked FTIR ATR spectra for all biochars with a baseline correction performed to show the peaks present, uncorrected spectra are shown in Figure S3. Low-intensity FTIR signals with a baseline shift at low wavenumbers have previously been attributed to aromatic carbon structures [57] and have previously been observed in both lignin-derived biochars and carbon black [10]. The C=C or methoxyl group (Me) peak indicated at 1420 cm^{-1} is associated with the presence of lignin monomers and indicates that the original lignin structure has not fully degraded in AL900, AL1100, DAL900, DAL1100, and HL900. A peak at approximately 1118 cm^{-1} corresponding to Na_2SO_4 or Na_2SO_3 is seen in all lignin-derived biochars, indicating that it does not fully degrade with pyrolysis at 1100 °C. No peaks were observed outside of the wavenumber range shown.

of S and Na are observed in non-lignin sourced biochars, with 0% S observed in CELL900, 0.16% S in WS900, and 0.12% S in WS1100 (Table 3). Only trace amounts of Mg, K, and Ca are observed in lignin- and cellulose-derived biochars, with higher content in WS-derived biochars. EDX measurements show high quantities of Si in WS-derived biochars, which was not quantified via ICP-OES in this study but was used to estimate oxygen content in WS-derived biochars. Limited inorganic carbon (IC) is expected in these biochars, as IC is primarily present as calcium carbonate or dolomite in biochars and low quantities of Ca and Mg are observed in all biochars measured in this study [55,56]. For all of the lignin biochars used in this study, IC is less than 1.5% of the total carbon (TC). Due to their higher Ca and Mg content, WS-derived biochars have higher IC content at around 7% of the TC.

In all biochars, ATR FTIR spectra show baseline shifts that have previously been attributed to polyaromatic carbon structures [10,19,57,58] (Fig. 6). Except for HL1100, all lignin-derived biochars showed the same primary peaks. The strong peak at approximately 1420 cm^{-1} has previously been attributed to methoxyl groups in lignin monomers [59] or C=C bonds in aromatic rings of lignin monomers [57,60]. The magnitude of this peak decreased with increasing pyrolysis temperature, indicating a loss of the original lignin structure at higher pyrolysis temperatures. The sharp peak observed at 876 cm^{-1} identifies the presence of C-H bonds associated with aromatic carbon rings [57,60]. This peak decreased with increasing pyrolysis temperature, a finding consistent with the decrease in H:C molar ratios observed at higher temperatures.

FTIR spectra of all lignin-based biochars indicated the presence of Na_2SO_4 and Na_2SO_3, as shown by the peak at 1118 cm^{-1}, the weak, broad peak at 2285 cm^{-1} and the overlapping peaks at 620

Table 3
Elemental analysis and ICP-OES results for all biochar. Results for C, H, N and S are an average of two measurements.

Biochar	C[†] (wt. %)	IC[††] (wt. %)	H[†] (wt. %)	N[†] (wt. %)	S[†] (wt. %)	Na (wt. %)	Mg (wt. %)	K (wt. %)	Ca (wt. %)	O (wt. %)	H:C (mol/mol)	O:C (mol/mol)
AL900	64.0	0.79	0.7	0.8	3.0	9.82	0.05	0.15	0.16	21.29	0.13	0.32
AL1100	70.6	0.92	0.6	0.7	3.0	8.07	0.08	0.15	0.20	16.17	0.10	0.21
CELL900	92.2	0.04	0.6	0.0	0.0	0.01	0.01	0.15	0.01	7.09	0.08	0.06
DAL900	65.2	0.92	0.7	0.6	4.8	10.57	0.14	0.15	0.08	17.68	0.13	0.25
DAL1100	69.4	1.04	0.4	0.5	5.5	8.91	0.14	0.15	0.09	15.00	0.07	0.17
HL900	71.5	0.18	0.7	0.7	4.0	6.79	0.01	0.15	0.05	15.88	0.12	0.18
HL1100	83.7	0.20	0.5	0.7	2.5	2.47	0.01	0.21	0.06	9.81	0.06	0.08
WS900	60.8	4.24	1.2	1.0	0.2	0.01	0.44	2.86	0.71	13.57[‡]	0.23	0.17
WS1100	60.7	4.34	0.7	1.0	0.1	0.13	0.43	3.10	0.77	13.65[‡]	0.13	0.17

[†] C, H, N and S values are an average of two measurements. [††] IC values are calculated from the Mg and Ca ICP-OES data and calculations based on the assumption that they are in the form of carbonates [55,56]. [‡] WS oxygen content was estimated as described in Section 2.4.2.

and 660 cm^{-1} [61–63] (Figure ATR). Elemental analysis, ICP-OES, and EDX confirm high quantities of both Na and S. As Na_2SO_4 and Na_2SO_3 is used in the kraft lignin isolation process [37,64], the presence of this band indicates that some Na_2SO_4 or Na_2SO_3 from the lignin isolation process remains after lignin pyrolysis. This finding is supported by past studies of lignin pyrolysis, which have indicated the formation of Na_2SO_3 crystalline regions in lignin-derived biochar [63,65].

In contrast to AL- and DAL-derived biochars, FTIR spectra show a shift in structure in HL-derived biochars as pyrolysis temperature increases from 900 °C to 1100 °C (Fig. 6, green). The strong peak associated with lignin monomers (1421 cm^{-1}) was reduced, and new peaks were seen at 1558 and 1507 cm^{-1}, which are caused by C=C stretching associated with aromatic carbon, and aromatic skeleton vibrations respectively [17,57,64]. This shift in the FTIR spectra indicates that a reordering of the original aromatic lignin structure has occurred between 900 °C and 1100 °C in HL-derived biochar. The broad Na_2SO_4 or Na_2SO_3 peak (1118 cm^{-1}) is lower in magnitude than the other lignin-derived biochars. Along with observed decreases in Na and S concentrations, the decreased magnitude of Na_2SO_4 in HL1100 indicates that some of the Na_2SO_4 seen in other lignin biochars has reacted during the pyrolysis of HL1100.

WS900, WS1100, and CELL900 biochars all exhibit few, low absorbance peaks, indicating a largely graphitic structure with few functional groups [19,66]. The presence of an Si–O peak (1082 cm^{-1}) in WS900 and WS1100 differentiates the infrared spectra of WS-derived biochars from those of other feedstocks [64]. The WS-derived biochars also show a C=C aromatic out of plane bending peak at around 799 cm^{-1} [17] and few additional peaks, indicating a highly graphitic carbon structure.

Raman spectra of all biochar examined show both D and G peaks characteristic of disordered graphitic carbon. As highly crystalline graphite exhibits very little or no intensity of the D peak, this peak indicates smaller graphitic crystallites and the presence of edge defects or oxygen functional groups on the aromatic carbon structure [10,19]. The size of graphitic crystallites is inversely related to the ratio of the intensities of the D and G peaks (I_{DG}) [42,67]. As increasing graphite crystallite size drives electric percolation in non-graphitizing carbons [58], decreasing I_{DG} ratio is expected to lead to an increase in electrical conductivity of the biochar. AL and DAL-derived biochars both increase in I_{DG} ratio with increasing pyrolysis temperature, while HL-derived biochars decrease (Fig. 7, top right). As decreasing I_{DG} ratio is expected to correlate with increased electrical conductivity, the increase in I_{DG} ratio in AL and DAL as the pyrolysis temperature increases from 900 °C to 1100 °C may contribute in part to their non-significant change in electrical conductivity. In contrast, WS and HL-derived biochars show only a small change and a decrease in I_{DG} ratio respectively as pyrolysis temperature increases from 900 °C to 1100 °C, and both show a statistically significant increase in electrical conductivity.

In addition to changes in intensity, apparent shifts in Raman peak position and width can indicate changes in the graphitic structure. An apparent G peak location below 1582 cm^{-1} is seen in all biochars measured in this study. This peak shift has previously been associated with the presence of amorphous carbon, with increasing amorphous carbon content further decreasing the apparent peak location [42,68]. Additionally, the increased width of the G peak is associated with the growing presence of bond angle disorder in sp^2 carbons [42]. Except for AL-derived biochar, all biochars measured in this study decrease in G peak width with increasing pyrolysis temperature (Fig. 7, bottom right). Together, these results indicate that a more ordered polyaromatic carbon structure is formed at higher pyrolysis temperatures in most biochars examined in this study.

Biochars observed in this study primarily show resistive AC behavior, which has previously been associated with graphitic carbon, while capacitive behavior is related to the presence of amorphous carbon [69]. The limited capacitive behavior observed in biochars in this study indicates that percolation has occurred between low impedance, resistive graphitic carbon regions [19,58].

3.4. Biochar physical structure

The morphological structure of the biochars obtained in this study was examined with FESEM imaging (Fig. 8). FESEM images show WS900 and WS1100 biochars having larger particle sizes than the lignin or cellulose sourced biochars, with the original fiber structure of these materials maintained. Higher magnification imaging shows WS-derived biochars to have a smoother surface than the lignin- or cellulose-derived biochars.

Particle size measurements supported the FESEM findings; WS-derived biochars exhibited a larger particle size than most lignin-derived biochars (Table 4). HL1100 and CELL900 show average particle sizes of approximately 5 μm. While these two biochars are the smallest size of any measured in this study, their average size is around two orders of magnitude larger than carbon black [70]. Particle size distributions are shown in Figure S10. Biochar with smaller particle sizes may be favorable for electrical applications, as electrical percolation thresholds in carbon-filled polymers have been established to decrease with decreasing particle size [71,72]. Additionally, decreasing particle size is associated with increased mechanical properties of nanofilled composites [73]. Past studies of biochar have examined spray-drying and hydrothermal treatment methods, obtaining biochar particles as small as 21.7 nm [12,16]. Further ball milling of lignin-derived biochars has shown only minor reductions in particle size [10]. Future work should examine the impact of these treatments on lignin-derived biochar to see if further decreases in particle size can be obtained for these materials.

Biochar surface area was observed to vary by feedstock and pyrolysis temperature. CELL900 has the highest surface area of the biochars produced in this study at 480 m^2/g. Except for HL1100, all lignin biochars in this study have surface areas between 10.1 and 27 m^2/g. Small decreases in surface area are observed with increasing pyrolysis temperature for AL-, DAL-, and WS-derived biochars. In contrast, HL-derived biochars show an increase in surface area from 18 to 109 m^2/g as pyrolysis temperature increases from 900 °C to 1100 °C. Both WS900 and WS1100 biochars show higher surface areas than all lignin biochars except HL1100. Past work has established feedstock lignin content to be inversely correlated with BET surface area in biochar [74]. The results herein support this finding, except for HL1100, providing additional evidence supporting the hypothesis that a shift in structure occurs in HL sourced biochars from 900 °C to 1100 °C, which is not present in the other biochars.

Biochar pore size distributions show that, despite apparent changes in primary pore size in HL1100, only minor changes are seen in pore size distribution (Figure S8). For most biochars, the smallest pores present in the biochars produced at 1100 °C are not observed in the 900 °C biochars, indicating that changes in porosity between 900 °C and 1100 °C are due to the formation of pores less than 20 Å in size produced between these temperatures.

In most measurements in this study, HL-derived biochars demonstrate different behavior than AL- or DAL-derived biochars. These differences include meaningfully different FTIR spectra, the highest carbon content, the highest surface area, the lowest O:C and H:C molar ratios, and the lowest content of all metals. In HL-derived biochars I_{DG} ratio decreases as pyrolysis temperature increases from 900 °C to 1100 °C indicating additional graphitization, while AL and DAL-derived biochars show a small increase in I_{DG}

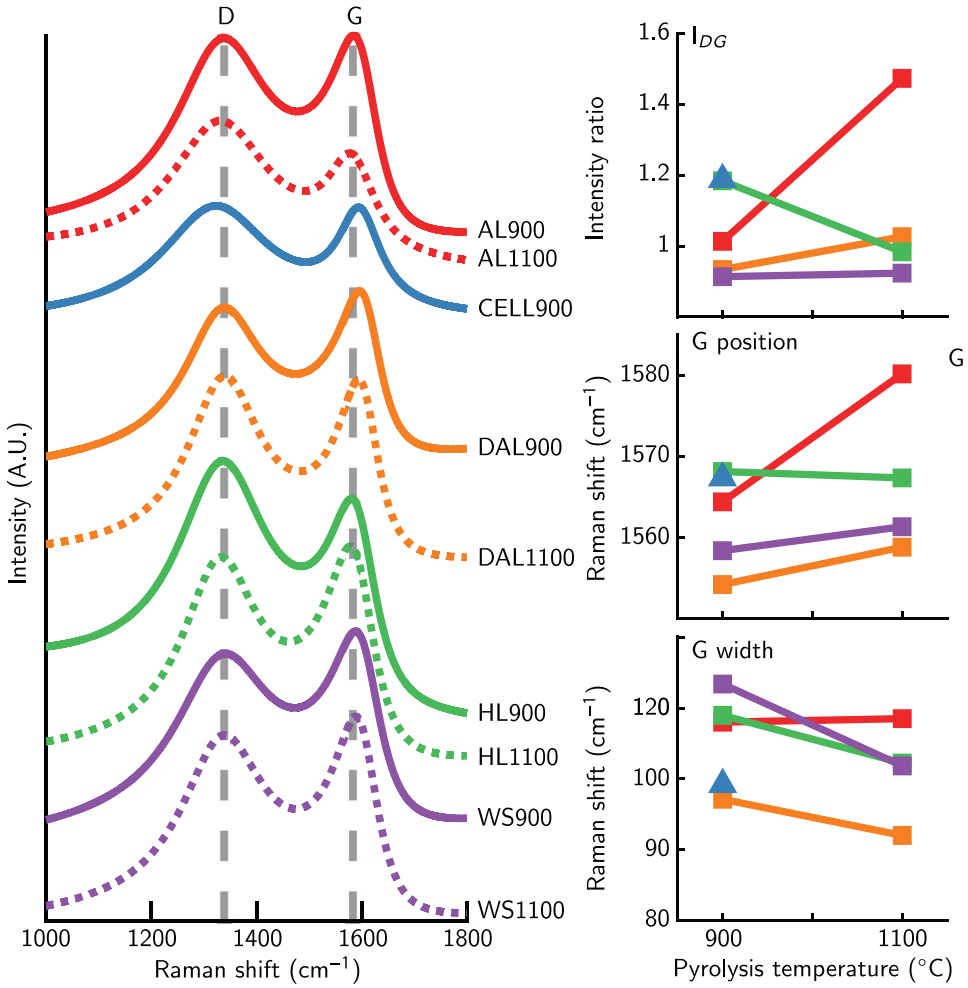

Fig. 7. (Left) An average of the three replicate fit Raman spectra for all biochars. The representative positions of D (1340 cm^{-1}) and G peaks (1582 cm^{-1}) are shown. Fits are a combination of a Lorentzian peak (D, centered on 1340 cm^{-1}) and a BWF peak (G, centered on 1582 cm^{-1}). Additional Raman spectra replicates, as well as the curve fitting process, are shown in Figure S4-S7. (Right) The average difference in the ratio of D and G intensities for each biochar (top), average shift relative to the characteristic position for the G band for each biochar with the characteristic position shown by the grey dashed line (middle), and width of the G band for each biochar (bottom). The line colors for the right figures represent the same feedstocks as in the left figure. Values for D-position, G-position, and I_{DG} ratio are shown in Table S3. (For interpretation of the references to colour in this figure legend, the reader is referred to the web version of this article.)

Table 4
Surface area and primary pore size as measured by nitrogen adsorption and average particle size as measured by particle size analysis.

Biochar	Surface area (m^2/g)	Primary pore size (Å)	Average particle size (μm)
AL900	27.0	32.9	13.1
AL1100	21.2	10.9	12.0
CELL900	480.2	8.4	4.9
DAL900	11.5	26.2	14.0
DAL1100	10.7	10.9	15.0
HL900	18.0	10.9	19.1
HL1100	109.1	7.9	5.5
WS900	86.8	11.0	62.0
WS1100	75.9	11.0	130

ratio with increasing pyrolysis temperature. Additionally, it shows the highest electrical conductivity of any biochar measured in this study. These findings support that a transition in biochar structure has occurred between 900 °C and 1100 °C in HL-derived biochars that benefits electrical conductivity. Between 900 °C and 1100 °C, HL-derived biochar loses the lignin-monomer peaks at 1420 and 876 cm^{-1} seen in HL900 and all other lignin-derived biochars, transitions from 17.97 to 109.1 m^2/g surface area, and loses over half its metal content. In contrast, AL- and DAL-derived biochars decrease in surface area, gain in relative metal content, and show only minor changes in FTIR spectra between these temperatures. This change in HL between 900 °C and 1100 °C does not correspond to a change in TGA slope or any shift in pyrolysis gases released, as measured by TGA-IR. Therefore, we hypothesize that this transition is primarily due to a reordering of the carbon structure of HL between 900 °C and 1100 °C, as indicated by Raman spectroscopy. While the mechanisms behind this shift are not yet fully understood, we hypothesize that shifts in lignin oxygen content, molecular weight, and metal content may be responsible for this shift in pyrolysis behavior.

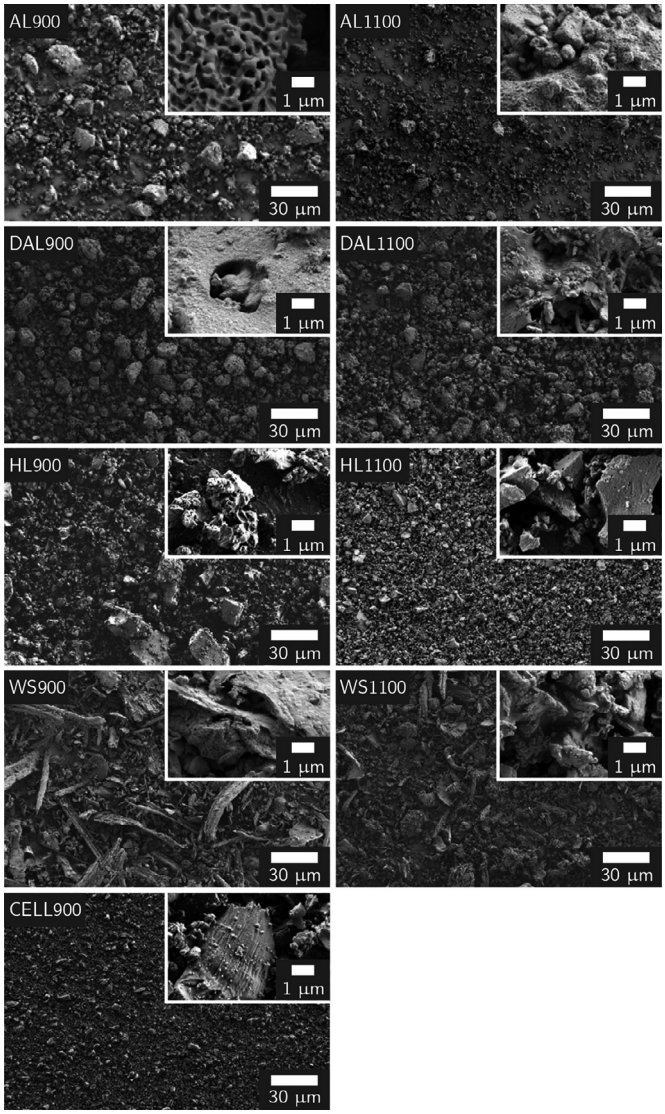

Fig. 8. FESEM images of biochar produced from all feedstocks and pyrolyzed at 900 °C (left) and 1100 °C (right). Images were acquired at a magnification of 1000× for the main image and 25k× for the inset. Scale bars are 30 μm for the main image and 1 μm for the inset.

3.5. Relationship between chemical and structural properties of biochar and electrical conductivity

The best fit estimated model determined through a forward, step-wise *p*-value model selection process, considering O:C molar ratio, H:C molar ratio, inorganic content, particle size (PS), surface area and I_{DG}, is defined as:

$$\sqrt{\hat{\sigma}\text{max}_{ijk}} = 3.18 - 8.55(\text{O:C}_i) + 3.13(\text{PS}_i^*) + 7.14(\text{PS}_i^*)^2 \qquad (1)$$

where $\sqrt{\hat{\sigma}\text{max}_{ijk}}$ is the square root of the mean maximum conductivity of the *k*th time observation in the *j*th sample in the *i*th treatment and PS_i^* relates to the orthogonal polynomial terms for biochar particle size for each treatment *i* (see Section 2.6 and Section S2.2 of the supplemental information for a complete model definition, additionally the full code used to generate this model is available [50]).

Accounting for the random effects sample and time observation and all other respective model terms, strong evidence exists to support a change in the mean $\sqrt{\sigma_{\text{max}}}$ as the O:C molar ratio changes ($t(5)$=-4.448 with an associated *p*-value=0.0067; standard error (SE) 1.12) and moderate evidence exists to support a change in the mean $\sqrt{\sigma_{\text{max}}}$ as the biochar particle size changes ($t(5)$=2.803 with an associated *p*-value=0.038; SE 2.5). An effects plot shows a notable decrease in $\sqrt{\sigma_{\text{max}}}$ as the O:C ratio increases. For particle size below approximately 60–70 μm, $\sqrt{\sigma_{\text{max}}}$ decreases as particle size increases. Above 60–70 μm, $\sqrt{\sigma_{\text{max}}}$ begins to increase with increasing particle size (Fig. 9).

Statistical analyses of the relationship between biochar properties and electrical conductivity were limited by the lack of true replicates for each biochar, as only one batch of material was considered for each treatment. Further, this study was an incomplete factorial design, as CELL1100 produced no biochar. These limitations prevented consideration of interactions during the modeling process. Results may not apply to measurements outside the O:C molar ratio (0.06-0.32) and particle size (4.9–130 μm) observed in this study. Lack of random assignment and random sampling in the experimental design prohibits any causal inference or generalization of results beyond data observed in this study.

The reduction in electrical conductivity with increasing oxygen content observed in this study is strongly supported by past literature. The presence of oxygen in non-graphitizing carbons results in distortions in the graphitic structure and increases the presence of sp^3 hybridized carbons. These distortions are expected to reduce the electrical conductivity of the resulting material [58]. Further, the presence of surface oxygen in carbon blacks has been associated with a decrease in electrical conductivity [3]. The model examined in this study does not examine the impacts of inorganic oxygen content, which FTIR spectra show to be present in the form of Na_2SO_4 or Na_2SO_3 in lignin-derived biochars and as Si–O in wheat stem-derived biochar. As these inorganic oxygen groups do not form distortions in the graphitic carbon structure, they are expected to be less impactful on electrical conductivity than organic oxygen. Some factors that are expected to impact electrical conductivity, in particular carbon content and I_{DG} ratio, were not found to be statistically significant in this model. This may be due to oxygen content being a more predictive indicator of both these factors, as increased oxygen content is expected to result in a larger D peak [58] and decreased carbon content.

Past work has shown the electrical conductivity of packed carbon particles to increase with increasing particle size [75]. This increase in electrical conductivity has been attributed to decreased contact resistance between particles with large particles. In contrast, our results show increases in electrical conductivity at low particle sizes ($< 20\mu$m) and high particle sizes ($> 100\mu$m). Both WS900 and WS1100 biochars show oblong geometry rather than the approximately spherical geometry seen in other biochars (Fig. 8), a broader particle size distribution than was observed in other biochars (Figure S10), and are the two largest biochars measured in this study. Shifts in particle geometry and particle size distributions are expected to impact particle packing, and electrical conductivity of the packed powder [52,75]. Particle geometry and particle size distribution were not variables under consideration in this model as they covaried with particle size. As no other biochars show a particle size greater than 20 μm were examined in this study, examining more biochars of larger particle size would improve understanding of the electrical conductivity behavior of large particle size biochar.

A critical finding of this model is that despite the presence of relatively high quantities of sulfur, alkali metals, and alkaline-earth metals in lignin-derived biochars, inorganic content was not selected in the final, best-fit model. Some studies have proposed the presence of S and Na in lignin-derived biochar as a catalyst for the formation of graphitic regions in lignin-derived biochars [20,76], while other studies have proposed that the presence of Na inhibits the formation of graphitic regions [23]. Further investigation of the impacts of sodium sulfate and sulfite present on the pyrolysis of

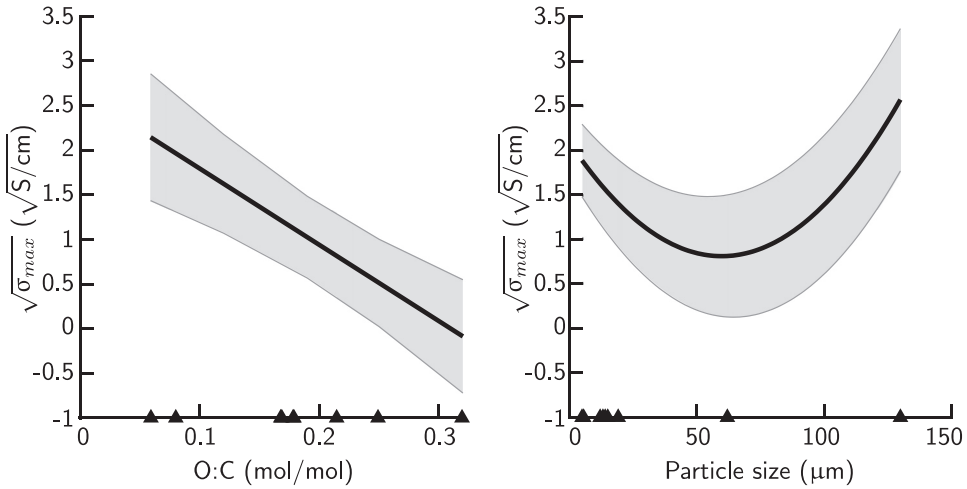

Fig. 9. Effects plots for the predictor variables O:C ratio (left) and particle size (right). ▲ symbols on the x axis show the position of O:C ratio and particle size observations. Shaded regions represent an estimated 95% confidence interval.

lignin is needed to better understand the role they play in lignin pyrolysis.

Lignin-derived biochar measured in this study, and particularly HL1100, show promising electrical conductivity as an alternative to carbon black [34]. This study demonstrates that even in lignin isolated with similar processes, wide variations in electrical conductivity exist in lignin-derived biochars. Therefore, careful selection of lignin feedstocks is needed to produce highly electrically conductive lignin-derived biochar. Based on the results of this study, we hypothesize that reductions in oxygen content of the lignin feedstock may allow for further optimization of lignin-derived biochar electrical conductivity. This reduction may be achieved by select modification of lignin monomers and linkages to reduce the oxygen content in the feedstock lignin. Optimization of pyrolysis conditions, including maximum temperature, ramp rate, and added catalysts may further reduce oxygen content in lignin-derived biochars. Reduction in oxygen content in lignin-derived biochar will allow for the formation of larger graphitic regions and further improvements in lignin-derived biochar conductivity [18,19,58]. Spray-drying methods may achieve further reductions in biochar particle size, with studies examining spray-drying of lignin-derived biochars obtaining particles similar in size to common carbon blacks [12,16]. We hypothesize that further reductions in biochar particle size may benefit biochar electrical behavior by increasing electrical conductivity and improving percolation behavior in composite materials.

4. Conclusions

The key finding of this study is that, when controlling for heating rate, catalysts added, and electrical conductivity measurement method, large variations are still seen in the electrical conductivity of biochar produced from lignin feedstocks isolated with similar processes. The wide range of electrical conductivity observed for lignin-derived biochar in this study demonstrates that careful selection of lignin feedstocks is key to producing highly electrically conductive biochar. We demonstrate a maximum conductivity of 18.5 S/cm from a laboratory isolated lignin used as a feedstock for biochar processed at 1100 °C. A shift in biochar structure is seen between pyrolysis temperatures of 900 °C and 1100 °C for HL, the highest electrical conductivity feedstock examined in this study. Further examination of the mechanisms behind this shift may enable the identification of lignin isolation processes to produce highly electrically conductive lignin-derived biochars.

This study found that lignin-derived biochar can obtain a similar range of conductivities to carbon black. Therefore, careful tuning of biochar properties could allow lignin-derived biochar to fulfill many of the current applications of carbon black. This work highlights the further reduction in oxygen content as an area for potential future improvements in the electrical conductivity of lignin-derived biochar. Careful selection of biomass sources for lignin isolation and lignin isolation processes may reduce biochar oxygen content, potentially allowing for the development of highly electrically conductive biochars for use as a filler material in energy storage applications.

Funding

Primary funding for this work was through startup funds from Montana State University. This work was performed in part at the Montana Nanotechnology Facility, a member of the National Nanotechnology Coordinated Infrastructure (NNCI), which is supported by the National Science Foundation (Grant #ECCS-1542210). Statistical contributions were funded through the Montana Partnership for Enhancing Mathematical Knowledge and Statistical Skills (MT PEAKS) by the National Science Foundation (Grant #DMS-1748883). Graduate fellowship support for Seth Kane was provided by the Environmental Research & Education Foundation's Ph.D. Scholarship. Undergraduate research was supported by the Undergraduate Scholars Program (USP) at Montana State University.

Declaration of Competing Interest

The authors declare that they have no known competing financial interests or personal relationships that could have appeared to influence the work reported in this paper.

Acknowledgements

The authors would like to thank Dr. Robin Gerlach and Abby Thane for assistance with and analytical instruments for TGA measurements. Dr. David Hodge and Dr. Sandip Singh generously provided lignin for this study as well as consultation regarding its isolation. The authors would also like to thank Dr. Stephan Warnat for providing additional consultation on statistical methods and advice on and instrumentation for testing the conductivity of powders. The Montana State University Environmental Analytical Lab

provided essential support by running ICP-OES measurements. Finally, we would like to thank Dr. Mark Greenwood and Dr. John Borkowski for their contributions to the statistical analyses.

Supplementary material

Supplementary material associated with this article can be found, in the online version, at doi:10.1016/j.cartre.2021.100088.

References

[1] A. Rahman, S. Al-Zahrani, I. Ali, S.M.A. Zahrani, R.H. Eleithy, A review of the applications of nanocarbon polymer composites, NANO Brief Rep. Rev. 6 (2011) 185–203, doi:10.1142/S179329201100255X. https://www.researchgate.net/publication/236668728.

[2] A.S. Aricó, P. Bruce, B. Scrosati, J.M. Tarascon, W.V. Schalkwijk, Nanostructured materials for advanced energy conversion and storage devices, Nat. Mater. 4 (2005) 366–377. https://www.nature.com/articles/nmat1368. www.nature.com/naturematerials.

[3] D. Pantea, H. Darmstadt, S. Kaliaguine, L. Sümmchen, C. Roy, Electrical conductivity of thermal carbon blacks: influence of surface chemistry, Carbon 39 (2001) 1147–1158, doi:10.1016/S0008-6223(00)00239-6.

[4] W. Zhang, A.A. Dehghani-Sanij, R.S. Blackburn, Carbon based conductive polymer composites, J. Mater. Sci. 42 (2007) 3408–3418, doi:10.1007/s10853-007-1688-5. https://link.springer.com/article/10.1007/s10853-007-1688-5.

[5] Z. Han, H. Li, J. Xiao, H. Song, B. Li, S. Cai, Y. Chen, Y. Ma, X. Feng, Ultralow-cost, highly sensitive, and flexible pressure sensors based on carbon black and airlaid paper for wearable electronics, ACS Appl. Mater. Interfaces 11 (36) (2019) 33370–33379, doi:10.1021/acsami.9b12929.

[6] S.S. Siwal, Q. Zhang, N. Devi, V.K. Thakur, Carbon-based polymer nanocomposite for high-performance energy storage applications, Polymers 12 (3) (2020), doi:10.3390/polym12030505. https://www.mdpi.com/2073-4360/12/3/505.

[7] R.J. Gosselink, E.D. Jong, B. Guran, A. Abächerli, Co-ordination network for lignin - standardisation, production and applications adapted to market requirements (EUROLIGNIN), Ind. Crops Prod. 20 (2004) 121–129, doi:10.1016/j.indcrop.2004.04.015.

[8] I. Norberg, Carbon fibers from kraft lignin, KTH, School of Chemical Science and Engineering (CHE), Fibre and Polymer Technology, Wood Chemistry and Pulp Technology, Stockholm: KTH Royal Institute of Technology, 2012 Ph.D. thesis.

[9] J. Lehmann, S. Joseph, Biochar for Environmental Management, Science, and Technology, Earthscan, 2009.

[10] M.R. Snowdon, A.K. Mohanty, M. Misra, A study of carbonized lignin as an alternative to carbon black, ACS Sustain. Chem. Eng. 2 (5) (2014) 1257–1263. https://pubs.acs.org/doi/10.1021/sc500086v. https://pubs.acs.org/sharingguidelines.

[11] M.Z. Rahman, T. Edvinsson, P. Kwong, Biochar for electrochemical applications, Curr. Opin. Green Sustain. Chem. 23 (2020) 25–30, doi:10.1016/j.cogsc.2020.04.007.

[12] S.M. Jasim, N.A. Ali, Properties characterization of plasticized polylactic acid /biochar (bio carbon) nano-composites for antistatic packaging, Iraqi J. Phys. 17 (2019) 13–26, doi:10.20723/ijp.17.42.13-26.

[13] M. Demir, Z. Kahveci, B. Aksoy, N.K. Palapati, A. Subramanian, H.T. Cullinan, H.M. El-Kaderi, C.T. Harris, R.B. Gupta, Graphitic biocarbon from metal-catalyzed hydrothermal carbonization of lignin, Ind. Eng. Chem. Res. 54 (43) (2015) 10731–10739, doi:10.1021/acs.iecr.5b02614.

[14] V. Hoffmann, D. Jung, J. Zimmermann, C.R. Correa, A. Elleuch, K. Halouani, A. Kruse, Conductive carbon materials from the hydrothermal carbonization of vineyard residues for the application in electrochemical double-Layer capacitors (EDLCs) and direct carbon fuel cells (DCFCs), Materials 12 (10) (2019) 1703, doi:10.3390/ma12101703. https://www.mdpi.com/1996-1944/12/10/1703.

[15] K. Mochidzuki, F. Soutric, K. Tadokoro, M.J. Antal, M. Tóth, B. Zelei, G. Várhegyi, Electrical and physical properties of carbonized charcoals, Ind. Eng. Chem. Res. 42 (21) (2003) 5140–5151, doi:10.1021/ie030358e. https://pubs.acs.org/sharingguidelines.

[16] N.K.R. Palapati, M. Demir, C.T. Harris, A. Subramanian, R.B. Gupta, Enhancing the electronic conductivity of Lignin-sourced, sub-micron carbon particles, in: 2015 IEEE Nanotechnology Materials and Devices Conference (NMDC), IEEE, 2015, pp. 1–2, doi:10.1109/NMDC.2015.7439257. http://ieeexplore.ieee.org/document/7439257/.

[17] P. Quosai, A. Anstey, A.K. Mohanty, M. Misra, Characterization of biocarbon generated by high- and low-temperature pyrolysis of soy hulls and coffee chaff: for polymer composite applications., R. Soc. Open Sci. 5 (8) (2018) 171970, doi:10.1098/rsos.171970. http://www.ncbi.nlm.nih.gov/pubmed/30224985 http://www.pubmedcentral.nih.gov/articlerender.fcgi?artid=PMC6124110.

[18] Y.R. Rhim, D. Zhang, D.H. Fairbrother, K.A. Wepasnick, K.J. Livi, R.J. Bodnar, D.C. Nagle, Changes in electrical and microstructural properties of microcrystalline cellulose as function of carbonization temperature, Carbon 48 (4) (2010) 1012–1024, doi:10.1016/j.carbon.2009.11.020.

[19] Y. Shao, C. Guizani, P. Grosseau, D. Chaussy, D. Beneventi, Biocarbons from microfibrillated cellulose/lignosulfonate precursors: a study of electrical conductivity development during slow pyrolysis, Carbon 129 (2018) 357–366, doi:10.1016/j.carbon.2017.12.037. https://linkinghub.elsevier.com/retrieve/pii/S0008622317312708.

[20] S. Vivekanandhan, M. Misra, A.K. Mohanty, Microscopic, structural, and electrical characterization of the carbonaceous materials synthesized from various lignin feedstocks, J. Appl. Polym. Sci. 132 (15) (2015) n/a–n/a, doi:10.1002/app.41786. http://doi.wiley.com/10.1002/app.41786.

[21] B. Wang, T. Shi, Y. Zhang, C. Chen, Q. Li, Y. Fan, Lignin-based highly sensitive flexible pressure sensor for wearable electronics, J. Mater. Chem. C 6 (24) (2018) 6423–6428, doi:10.1039/c8tc01348a. https://pubs.rsc.org/en/content/articlehtml/2018/tc/c8tc01348a https://pubs.rsc.org/en/content/articlelanding/2018/tc/c8tc01348a.

[22] J. Xia, N. Zhang, S. Chong, D. Li, Y. Chen, C. Sun, Three-dimensional porous graphene-like sheets synthesized from biocarbon via low-temperature graphitization for a supercapacitor, Green Chem. 20 (3) (2018) 694–700, doi:10.1039/c7gc03426a. https://pubs.rsc.org/en/content/articlehtml/2018/gc/c7gc03426a https://pubs.rsc.org/en/content/articlelanding/2018/gc/c7gc03426a.

[23] G. Xiao, M. Ni, R. Xiao, X. Gao, K. Cen, Catalytic carbonization of lignin for production of electrically conductive charcoal, J. Biobased Mater.Bioenergy 6 (2012) 69–74, doi:10.1166/jbmb.2012.1190. https://www.researchgate.net/publication/272214339.

[24] C. Zhao, Y. Shi, J. Xie, F. Lei, L. Zhang, Direct measurement of electrical conductivity of porous biochar monolith for supercapacitors, Mater. Res. Express 6 (9) (2019) 095526, doi:10.1088/2053-1591/ab326e.

[25] S. Arnold, A. Rodriguez-Uribe, M. Misra, A.K. Mohanty, Slow pyrolysis of bio-oil and studies on chemical and physical properties of the resulting new biocarbon, J. Clean. Prod. 172 (2016) 2748–2758, doi:10.1016/j.jclepro.2017.11.137.

[26] M. Demir, A.A. Farghaly, M.J. Decuir, M.M. Collinson, R.B. Gupta, Supercapacitance and oxygen reduction characteristics of sulfur self-doped micro/mesoporous bio-carbon derived from lignin, Mater. Chem. Phys. 216 (2018) 508–516, doi:10.1016/j.matchemphys.2018.06.008.

[27] M. Deraman, S. Zakaria, R. Omar, A.A. Aziz, Electrical conductivity of carbon pellets from mixtures of pyropolymer from oil palm bunch and cotton cellulose, Jpn. J. Appl. Phys. 39 (12 A) (2000) L1236, doi:10.1143/jjap.39.l1236. https://iopscience.iop.org/article/10.1143/JJAP.39.L1236 https://iopscience.iop.org/article/10.1143/JJAP.39.L1236/meta.

[28] R.S. Gabbi, D.W. Kirk, C.Q. Jia, Preliminary investigation of electrical conductivity of monolithic biochar, Carbon 116 (2017) 435–442, doi:10.1016/J.CARBON.2017.01.069. https://www.sciencedirect.com/science/article/pii/S0008622317300799#fig4.

[29] R. Gabbi, L. Basile, Donald, W. Kirk, M. Giorcelli, A. Tagliaferro, Charles, Q. Jia, Electrical conductivity of wood biochar monoliths and its dependence on pyrolysis temperature, Biochar 2 (2020) 369–378, doi:10.1007/s42773-020-00056-0.

[30] M. Giorcelli, M. Bartoli, Development of coffee biochar filler for the production of electrical conductive reinforced plastic, Polymers 11 (12) (2019) 1916, doi:10.3390/polym11121916. https://www.mdpi.com/2073-4360/11/12/1916.

[31] M. Giorcelli, P. Savi, A. Khan, A. Tagliaferro, Analysis of biochar with different pyrolysis temperatures used as filler in epoxy resin composites, Biomass Bioenergy 122 (2019) 466–471, doi:10.1016/j.biombioe.2019.01.007.

[32] J. Jiang, L. Zhang, X. Wang, N. Holm, K. Rajagopalan, F. Chen, S. Ma, Highly ordered macroporous woody biochar with ultra-high carbon content as supercapacitor electrodes, Electrochim. Acta 113 (2013) 481–489, doi:10.1016/j.electacta.2013.09.121.

[33] F. Jiang, Y. Yao, B. Natarajan, C. Yang, T. Gao, H. Xie, Y. Wang, L. Xu, Y. Chen, J. Gilman, L. Cui, L. Hu, Ultrahigh-temperature conversion of biomass to highly conductive graphitic carbon, Carbon 144 (2019) 241–248, doi:10.1016/j.carbon.2018.12.030.

[34] S. Kane, S. Warnat, C. Ryan, Improvements in methods for measuring the volume conductivity of electrically conductive carbon powders, Adv. Powder Technol. 32 (3) (2021) 702–709, doi:10.1016/j.apt.2021.01.016.

[35] A.K. Kercher, D.C. Nagle, Evaluation of carbonized medium-density fiberboard for electrical applications, Carbon 40 (8) (2002) 1321–1330, doi:10.1016/S0008-6223(01)00299-8.

[36] D. Pantea, H. Darmstadt, S. Kaliaguine, C. Roy, Electrical conductivity of conductive carbon blacks: influence of surface chemistry and topology, Appl. Surf. Sci. 217 (1–4) (2003) 181–193, doi:10.1016/S0169-4332(03)00550-6.

[37] TCI America, Lignin, Technical Report, 2021. https://www.tcichemicals.com/US/en/p/L0045.

[38] S.K. Singh, A.W. Savoy, Z. Yuan, H. Luo, S.S. Stahl, E.L. Hegg, D.B. Hodge, Integrated two-stage alkaline-oxidative pretreatment of hybrid poplar. Part 1: impact of alkaline pre-Extraction conditions on process performance and lignin properties, Ind. Eng. Chem. Res. 58 (35) (2019) 15989–15999, doi:10.1021/acs.iecr.9b01124.

[39] J. Arroyo, C. Ryan, Incorporation of carbon nanofillers tunes mechanical and electrical percolation in PHBV:PLA blends, Polymers 10 (12) (2018) 1371. http://www.mdpi.com/2073-4360/10/12/1371.

[40] J. Arroyo, Developments in electrically conductive bio-composites for use in additive manufacturing, Montana State University: Mechanical & Industrial, Bozeman Montana, 2019 Master's thesis. https://scholarworks.montana.edu/xmlui/handle/1/15520.

[41] L. Bokobza, J.L. Bruneel, M. Couzi, Raman spectroscopic investigation of carbon-based materials and their composites. Comparison between carbon nanotubes and carbon black, Chem. Phys. Lett. 590 (2013) 153–159, doi:10.1016/j.cplett.2013.10.071.

[42] A. Ferrari, J. Robertson, Interpretation of raman spectra of disordered and

amorphous carbon, Phys. Rev. B 61 (2000) 14095–14107, doi:10.1103/PhysRevB.61.14095. https://journals.aps.org/prb/abstract/10.1103/PhysRevB.61.14095.
[43] D. McGlamery, A.A. Baker, Y.-S. Liu, M.A. Mosquera, N.P. Stadie, Phonon dispersion relation of bulk boron-doped graphitic carbon, J. Phys. Chem. C 124 (42) (2020) 23027–23037, doi:10.1021/acs.jpcc.0c06918.
[44] F. Rouquerol, J. Rouquerol, K.S.W. Sing, Adsorption by Powders and Porous Solids Principles, Methodology and Applications, second ed., Academic Press, San Diego, CA, USA, 2014.
[45] D.A. Gómez-Gualdrón, P.Z. Moghadam, J.T. Hupp, O.K. Farha, R.Q. Snurr, Application of consistency criteria to calculate BET areas of micro- and mesoporous metal-organic frameworks, J. Am. Chem. Soc. 138 (1) (2016) 215–224, doi:10.1021/jacs.5b10266.
[46] R Core Team, R: a language and environment for statistical computing, 2020, https://www.r-project.org/.
[47] R.V. Lenth, P. Buerkner, M. Herve, J. Love, H. Riebl, H. Singmann, emmeans: Estimated Marginal Means, aka Least-Squares Means, 2020, https://cran.r-project.org/web/packages/emmeans/index.html.
[48] A. Kuznetsova, P. Brockhoff, R. Christensen, lmerTest package: tests in linear mixed effects models, J. Stat. Softw. 82 (13) (2017) 1–26, doi:10.18637/jss.v082.i13.
[49] J. Fox, S. Weisberg, An R Companion to Applied Regression, third ed., Sage Publications, Thousand Oaks, CA, 2019. https://socialsciences.mcmaster.ca/jfox/Books/Companion/.
[50] S. Kane, R. Ulrich, A. Harrington, N. Stadie, C. Ryan, Code in support of: physical and chemical mechanisms that influence the electrical conductivity of lignin-derived biochar, 10.5061/dryad.fj6q573v2
[51] H. Yang, R. Yan, H. Chen, D.H. Lee, C. Zheng, Characteristics of hemicellulose, cellulose and lignin pyrolysis, Fuel 86 (12–13) (2007) 1781–1788, doi:10.1016/j.fuel.2006.12.013.
[52] A. Celzard, J.F. Marêché, F. Payot, G. Furdin, Electrical conductivity of carbonaceous powders, Carbon 40 (15) (2002) 2801–2815, doi:10.1016/S0008-6223(02)00196-3.
[53] B. Kay Hyeok An, W. Seok Kim, Y. Soo Park, Y. Chul Choi, S. Mi Lee, D. Chul Chung, D. Jae Bae, S. Chu Lim, Y. Hee Lee, Y.H. Lee, K.H. An, W.S. Kim, Y.S. Park, Y.C. Choi, S.M. Lee, D.J. Bae, S.C. Lim, D.C. Chung, Supercapacitors using single-walled carbon nanotube electrodes, Adv. Mater. 13 (7) (2001), doi:10.1002/1521-4095.
[54] D.S. McLachlan, C. Chiteme, W.D. Heiss, J. Wu, Fitting the DC conductivity and first order AC conductivity results for continuum percolation media, using percolation theory and a single phenomenological equation, Physica B 338 (1) (2003) 261–265, doi:10.1016/j.physb.2003.08.003. Proceedings of the Sixth International Conference on Electrical Transport and Optical Properties of Inhomogeneous Media
[55] J.-H. Yuan, R.-K. Xu, H. Zhang, The forms of alkalis in the biochar produced from crop residues at different temperatures, Bioresour. Technol. 102 (3) (2011) 3488–3497, doi:10.1016/j.biortech.2010.11.018. https://www.sciencedirect.com/science/article/pii/S0960852410018201.
[56] T. Wang, M. Camps-Arbestain, M. Hedley, B.P. Singh, R. Calvelo-Pereira, C. Wang, T. Wang, M. Camps-Arbestain, M. Hedley, B.P. Singh, R. Calvelo-Pereira, C. Wang, Determination of carbonate-c in biochars, Soil Res. 52 (2014) 495–504, doi:10.1071/SR13177. https://www.publish.csiro.au/sr/SR13177
[57] M. Keiluweit, P.S. Nico, M. Johnson, M. Kleber, Dynamic molecular structure of plant biomass-derived black carbon (biochar), Environ. Sci. Technol. 44 (4) (2010) 1247–1253, doi:10.1021/es9031419.
[58] J.S. McDonald-Wharry, M. Manley-Harris, K.L. Pickering, Reviewing, combining, and updating the models for the nanostructure of non-graphitizing carbons produced from oxygen-containing precursors, Energy Fuels 30 (2016) 7811–7826, doi:10.1021/acs.energyfuels.6b00917.
[59] I. Bykov, Characterization of natural and technical lignins using FTIR spectroscopy, Luleå University of Technology: Department of and Chemical Engineering and Geosciences, Luleå, Sweden, 2008.
[60] J. Li, Y. Li, Y. Wu, M. Zheng, A comparison of biochars from lignin, cellulose and wood as the sorbent to an aromatic pollutant, J. Hazard. Mater. 280 (2014) 450–457, doi:10.1016/j.jhazmat.2014.08.033.
[61] National Institute of Standards and Technology, Sodium Sulfate, Technical Report, 2018. https://webbook.nist.gov/cgi/cbook.cgi?ID=B6000542&Mask=80#IR-Spec
[62] K. Nakamoto, Infrared and Raman Spectra of Inorganic and Coordination Compounds Part B: Applications in Coordination, Organometallic, and Bioinorganic Chemistry, fifth ed., John Wiley and Sons Inc., 1997.
[63] C. Zhang, Y. Shao, L. Zhang, S. Zhang, R.J. Westerhof, Q. Liu, P. Jia, Q. Li, Y. Wang, X. Hu, Impacts of temperature on evolution of char structure during pyrolysis of lignin, Sci. Total Environ. 699 (2020) 134381, doi:10.1016/j.scitotenv.2019.134381.
[64] B. Singh, M.C. Arbestain, J. Lehmann, Biochar: A Guide to Analytical Methods, CRC press, 2017.
[65] T. Wang, M. Camps-Arbestain, M. Hedley, Predicting C aromaticity of biochars based on their elemental composition, Org. Geochem. 62 (2013) 1–6, doi:10.1016/j.orggeochem.2013.06.012.
[66] V. Ţucureanu, A. Matei, A.M. Avram, FTIR spectroscopy for carbon family study, Crit. Rev. Anal. Chem. 46 (6) (2016) 502–520, doi:10.1080/10408347.2016.1157013. https://www.tandfonline.com/doi/full/10.1080/10408347.2016.1157013.
[67] M.A. Pimenta, G. Dresselhaus, M.S. Dresselhaus, L.G. Cançado, A. Jorio, R. Saito, Studying disorder in graphite-based systems by raman spectroscopy, Phys. Chem. Chem. Phys. 9 (2007) 1276–1290, doi:10.1039/B613962K.
[68] N. Hauptman, A. Vesel, V. Ivanovski, M.K. Gunde, Electrical conductivity of carbon black pigments, Dyes Pigm. 95 (1) (2012) 1–7, doi:10.1016/j.dyepig.2012.03.012. https://www.sciencedirect.com/science/article/pii/S014372081200068X.
[69] A.G. Pandolfo, A.F. Hollenkamp, Carbon properties and their role in supercapacitors, J. Power Sources (2006), doi:10.1016/j.jpowsour.2006.02.065.
[70] T. Jawhari, A. Roid, J. Casado, Raman spectroscopic characterization of some commercially available carbon black materials, Carbon 33 (1995) 1561–1565, doi:10.1016/0008-6223(95)00117-V.
[71] X. Jing, W. Zhao, L. Lan, The effect of particle size on electric conducting percolation threshold in polymer/conducting particle composites, J. Mater. Sci. Lett. 19 (2000) 377–379. https://www.researchgate.net/profile/Xinli-Jing/publication/225882770_Effect_of_particle_size_on_electric_conducting_percolation_threshold_in_polymerconducting_particle_composites/links/55c9a92508aeca747d672a63/Effect-of-particle-size-on-electric-conducting-percolation-threshold-in-polymer-conducting-particle-composites.pdf.
[72] K.S. Deepa, S.K. Nisha, P. Parameswaran, M.T. Sebastian, J. James, Effect of conductivity of filler on the percolation threshold of composites, Appl. Phys. Lett. 94 (2009) 142902, doi:10.1063/1.3115031. http://aip.scitation.org/doi/10.1063/1.3115031.
[73] H. Alter, Filler particle size and mechanical properties of polymers, J. Appl. Polym. Sci. 9 (1965) 1525–1531, doi:10.1002/app.1965.070090427. http://doi.wiley.com/10.1002/app.1965.070090427.
[74] J. Sun, F. Lian, Z. Liu, L. Zhu, Z. Song, Biochars derived from various crop straws: characterization and Cd(II) removal potential, Ecotoxicol. Environ. Saf. 106 (2014) 226–231, doi:10.1016/j.ecoenv.2014.04.042.
[75] B. Marinho, M. Ghislandi, E. Tkalya, C.E. Koning, G. de With, Electrical conductivity of compacts of graphene, multi-wall carbon nanotubes, carbon black, and graphite powder, Powder Technol. 221 (2012) 351–358, doi:10.1016/j.powtec.2012.01.024. Selected papers from 2010 AIChE Annual Meeting, https://www.sciencedirect.com/science/article/pii/S0032591012000277.
[76] J. Rodríguez-Mirasol, T. Cordero, J.J. Rodríguez, High-temperature carbons from kraft lignin, Carbon 34 (1) (1996) 43–52, doi:10.1016/0008-6223(95)00133-6.